Soft Matter

ROYAL SOCIETY OF CHEMISTRY

PAPER

View Article Online
View Journal | View Issue

Cite this: *Soft Matter*, 2022, **18**, 1666

Rapid, interface-driven domain orientation in bottlebrush diblock copolymer films during thermal annealing†

Bijal B. Patel,[a] Dylan J. Walsh,[a] Kush Patel,[a] Do Hoon Kim,[a] Justin J. Kwok,[b] Damien Guironnet[a] and Ying Diao*[a]

Favorable polymer-substrate interactions induce surface orientation fields in block copolymer (BCP) melts. In linear BCP processed near equilibrium, alignment of domains generally persists for a small number of periods (~4–6 D_0) before randomization of domain orientation. Bottlebrush BCP are an emerging class of materials with distinct chain dynamics stemming from substantial molecular rigidity, enabling rapid assembly at ultrahigh (>100 nm) domain periodicities with strong photonic properties (structural color). This work assesses interface-induced ordering in PS-*b*-PLA bottle*b*rush diblock copolymer films during thermal annealing between planar surfaces. To clearly observe the decay in orientational order from surface to bulk, we choose to study micron-scale films spanning greater than 200 lamellar periods. *In situ* optical microscopy and transmission UV-Vis spectroscopy are used to monitor photonic properties during annealing and paired with *ex situ* UV-Vis reflection measurement, cross-sectional scanning electron microscopy (SEM), and small-angle X-ray scattering (SAXS) to probe the evolution of domain microstructure. Photonic properties were observed to saturate within minutes of annealing at 150 °C, with distinct variation in transmission response as a function of film thickness. The depth of the highly aligned surface region was found to vary stochastically in the range of 30–100 lamellar periods, with the sharpness of the orientation gradient decreasing substantially with increasing film thickness. This observation suggests a competition between growth of aligned, heterogeneously nucleated, grains at the surface and orientationally isotropic, homogeneously nucleated, grains throughout the bulk. This work demonstrates the high potential of bottlebrush block copolymers in rapid fabrication workflows and provides a point of comparison for future application of directed self-assembly to BBCP ordering.

Received 16th November 2021,
Accepted 1st February 2022

DOI: 10.1039/d1sm01634b

rsc.li/soft-matter-journal

I. Introduction

Block copolymers (BCP) comprising chemically incompatible, covalently-linked segments have attracted significant attention for bottom-up fabrication due to their spontaneous self-assembly into regular nanostructures with predictable equilibrium morphologies[1,2] and domain periodicities (D_0) generally in the range of 5–50 nm (for linear block copolymers).[3] While the shape of microphase-separated domains in the bulk is largely determined by block chemistry and volume fraction through energy-minimizing considerations,[1] the larger-scale microstructure of block copolymers in both thin films and bulk is strongly dependent on processing pathways. As a result, a wealth of directed self-assembly (DSA) strategies have been developed for driving enhanced microdomain orientation, grain size, and assembly kinetics.[4,5] These include variations on thermal and solvent annealing, substrate patterning (grapho-/chemoepitaxy),[6] and a variety of thermal, mechanical, and electromagnetic gradient-based approaches.[4,7] Despite extensive study, key challenges remain in balancing processing complexity (and cost) with the increasing demands for precisely tailored microstructure for lithography[8] and emerging areas such as energy generation/storage,[9] nanoparticle scaffolds,[10] and novel optical applications.[11]

A complementary and growing approach towards expanding the processability of BCP films has been to modify the architecture of constituent polymeric blocks by introducing branching at one or more points along the contour to create nonlinear block copolymers.[12] Of these, molecular 'bottlebrush' block

[a] *Department of Chemical and Biomolecular Engineering, University of Illinois at Urbana-Champaign, 600 South Mathews Avenue, Urbana, IL 61801, USA. E-mail: yingdiao@illinois.edu*
[b] *Department of Materials Science and Engineering, University of Illinois at Urbana–Champaign, 1304 W. Green Street, Urbana, Illinois 61801, USA*

† Electronic supplementary information (ESI) available. See DOI: 10.1039/d1sm01634b

copolymers (BBCP) have emerged as strong candidates for rapid self-assembly. BBCP exhibit a hierarchical structure of densely grafted linear block copolymer arms attached to a common backbone.[13] With increasing side chain length and grafting density, steric repulsion between adjacent side chains of the same molecule induces increased molecular rigidity and causes the overall molecule to behave as a semiflexible filament with substantially reduced entanglements in the melt[14,15] and limited interpenetration of flexible side chains[16] compared to the well-studied coil-like conformation of linear BCP. The distinct shape-persistence of BBCP is anticipated to have a pronounced impact on both dynamic and equilibrium self-assembly behavior.

Studies over the past decade have revealed much about the fundamentals of self-assembly for lamellae-forming BBCP prepared by melt annealing and slow solution casting. Notably, it is well established that the equilibrium scaling exponent of domain size (D_0) with backbone length (N_{bb}) is substantially higher for bottlebrush polymers ($\alpha \approx 0.8$–0.9)[13,17] than for strongly segregated linear block copolymers ($\alpha \approx 2/3$),[18] suggesting that molecular backbones indeed adopt more extended conformations than linear analogues. More recent theoretical and experimental works have clarified that BBCP in melt do, however, retain significant flexibility, with the Kuhn length of the backbone approximately equal to the overall molecular diameter.[19–21]

One very useful attribute of BBCP with domain sizes on the order of 100 nm and suitable refractive index contrast is the formation of a photonic band gap upon self-assembly (causing structural color).[22–28] Studies have demonstrated modulation of the photonic band gap across the visible to infrared spectrum by varying bottlebrush molecular weight[25] blend composition with bottlebrush,[29] homopolymer,[30] or nanoparticle additives,[31] and by tuning processing conditions during solution casting.[26] The direct connection between microstructure and optical properties (primarily reflection) has been used to evaluate ordering in photonic BBCP films by comparison predicted wavelength and reflectance of a 1D Bragg Stack.[22] More recently, confined self-assembly of BBCP within emulsified microdroplets has been reported as a route towards preparation of photonic crystals with reduced angular wavelength dependence,[24] and switchable color,[32] with interfacial effects strongly modifying domain orientation.

Interestingly, although many researchers have commented on the potential for bottlebrush block copolymers to exhibit substantially faster assembly into large well-ordered structures compared to their linear analogues, there are few published works that have investigated the evolution of BBCP microstructure over time or have quantified the extent of ordering compared to linear BCP. Using *in situ* SAXS, Gu, Russell, *et al.*,[17] monitored the self-assembly of bulk (~mm thickness) lamellae-forming PS-*b*-PLA at 130 °C and observed higher-order reflections forming at timescales of 5 minutes (M_n = 105 kg mol^{-1}) to 1 hour (M_n = 529 kg mol^{-1}), depending on the overall size of the molecule. Song, Watkins, *et al.*[33] in 2015 also use SAXS to demonstrate rapid ordering of large (M_n = 1850 kg mol^{-1}) BBCP in the bulk (1 mm thickness) after 5 minutes of annealing at 110 °C for low-T_g poly(*tert*-butyl acrylate)-*b*-poly(ethylene oxide) [PtBA-*b*-PEO,], and use a rastering SAXS approach to identify ordered, mm-scale grains.

The orientation of anisotropic BCP domains is substantially affected by the relative strength of interactions between each block and the confining surfaces. When the surface-polymer interactions for each block are balanced ('neutral'), BCP can adopt surface-perpendicular domain orientation, a behavior frequently achieved by grafting random copolymers of matching chemistry to the substrate. Preferential ('non-neutral') surfaces, as used here, instead induce surface-parallel domain orientation, where one block chemistry preferentially wets the substrate interface.[34,35] The penetration depth of surface-induced orientation fields has been found to be very system dependent, with reports ranging from 4–6 domain periods[36,37] to over 40 periods.[38] Several works have systematically varied the strength of substrate-polymer interactions to demonstrate control the propagation depth of surface oriented microdomains, generally concluding that increasing the polymer-substrate interfacial energy difference increases propagation depth.[36,37,39,40] Decreasing BCP molecular weight[41] or increasing annealing temperature[42] have also been reported to increase propagation depth by increasing molecular mobility to allow domain reorganization.

In this work, we consider interfacial ordering and confinement effects during rapid thermal annealing of a large (M_n = 1800 kg mol^{-1}) bottlebrush block copolymer system confined between hard interfaces at thicknesses in between the typical thin-film (submicron) and bulk (> mm) scale. These intermediate length scales (order of tens to hundreds of μm, or ~270–1700 lamellar periods) are of substantial relevance for both micro-extrusion based additive manufacturing[26] and common rheometric measurement geometries, and this method parallels the most commonly reported approach for preparing thermally annealed BBCP for photonic property characterization (compression between clamped glass slides). Thus, we believe that characterization of the spontaneous surface-induced ordering at these length scales provides a vital point of comparison for further work on direct self-assembly of bottlebrush block copolymers and a deeper understanding of prior work on large photonic-crystal forming BBCP.

II. Experimental methods

a. Materials synthesis and characterization

Well-defined poly(styrene)-*b*-poly(lactic acid) (PS-*b*-PLA) diblock bottlebrushes were produced *via* a previously developed route (Fig. 1a).[26,28,43] In brief, the methodology involves the synthesis of PS macromonomers *via* an anionic polymerization of styrene initiated by *sec*BuLi (M_n: 4500 g mol^{-1}, $Đ$: 1.03) and PLA macromonomers *via* an organocatalyzed 1,8-diazabicyclo-[5.4.0]undec-7-ene (DBU) ring opening polymerization of lactide (M_n: 4200 g mol^{-1}, $Đ$: 1.06).[28,44–49] Sequential addition ring-opening metathesis polymerization (ROMP) was then used

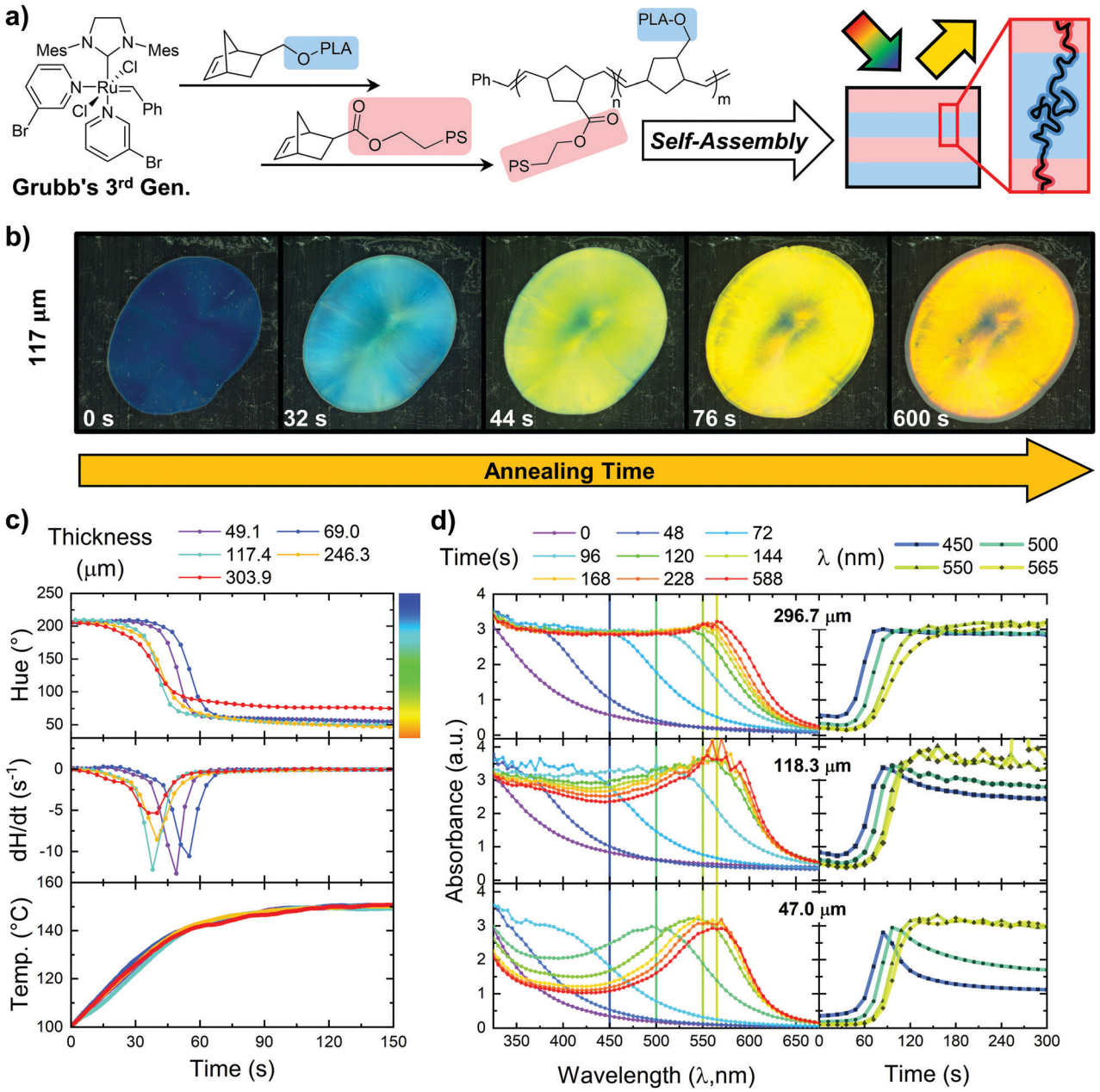

Fig. 1 Sample preparation and optical property evolution during annealing. (a) Simplified reaction scheme for synthesis of PS-*b*-PLA diblock bottlebrushes *via* sequential addition ROMP of PS and PLA macromonomers, along with cartoon of self-assembly into lamellar photonic crystals. Inset highlights the bilayer configuration of BBCP backbones within lamellae. (b) Microscope camera images showing the change of structure color during annealing for a 117.4 µm thick film. The inset text notes the time elapsed since the cell reached 100 °C. (c) Extracted average hue, forward finite difference quotient of hue, and measured temperature of the annealing cell plotted against annealing time for BBCP films of varying thickness under the microscope camera. (d) Evolution of the transmission properties of BBCP films of varying thickness during annealing measured by *in situ* UV-Vis absorption spectroscopy. Panels at right track the evolution of intensity at wavelengths of 450, 500, 550, and 565 nm; corresponding roughly to the blue, cyan, green, and the peak wavelength.

to synthesize the targeted symmetric diblock bottlebrushes with a targeted total backbone length of 400 repeat units. Size exclusion chromatography (SEC) analysis of the synthesized diblock revealed a bimodal peak and residual macromonomer (unfunctionalized PS arms, 1 w%). The major peak was determined to be the targeted diblock polymer (94 w% of the sample).[43] It presented a narrow molecular weight distribution of M_w/M_n: 1.05 and light scattering SEC gave an absolute molecular weight of 1800 kg mol^{-1}. The smaller peak was determined to be PS bottlebrush. This polymer sample was used for the following material studies. Further details of the synthesis are provided in ESI,† Section 1. As-prepared PS-*b*-PLA BBCP exhibited glass transitions at 95.9 °C and 49.2 °C, attributed to the poly(styrene) and poly(lactic acid) blocks, respectively (ESI,† Section 2).

b. Film preparation and melt annealing

Glass substrates (VWR 48300-026) were solvent cleaned by sequential ultrasonication (VWR 97043-992) for 5 minutes each in toluene (Fisher Chemical T324-4), acetone (Fisher Chemical A18-4), and isopropanol (Fisher Chemical A451-4) before swabbing with fresh isopropanol and drying with a nitrogen gun. BBCP films were prepared by direct compression of the as-synthesized BBCP powder (precipitated from anhydrous methanol and vacuum dried). To reduce lateral spreading of the polymer melt during annealing and concomitant thickness change, powder samples were first 'pre-pressed' at 115 °C in a simple aluminum/stainless steel annealing cell (ESI,† Section 3) on a hot plate. The film thickness was defined by using a combination of machined metal spacers external to the glass slides, and (for films < 100 μm) by patterning square 'wells' onto the glass substrates from fully cured SU-8 photoresist (MicroChem). Pre-pressing was performed by inserting the glass-polymer-glass sandwich into the pre-heated annealing cell and slowly tightening the screws over a period of several minutes.

c. Annealing and optical characterization

Two sets of annealed samples were prepared to capture *in situ* evolution of optical properties in both reflection and transmission modes. For both sets, the annealing cell was assembled at room temperature and placed on top of a rectangular resistive heater (Rama Corporation M60B45S/DVZ10) powered through a closed-loop temperature controller (Watlow EZ-Zone) with a thermocouple affixed to the bottom plate of the annealing cell. Temperature data during the during a ramp/hold at 150 °C were recorded at 0.1 s intervals using a LabVIEW routine provided by the controller manufacturer. The PID controller was tuned to optimize heating rate and minimize overshoot independently for each of the configurations described below. All timepoints reported in this manuscript refer to the time elapsed after the cell reached 100 °C. All optical reflection/absorbance peaks were fit using an asymmetric Gaussian model in Origin (OriginLab Corporation).

***In situ* monitoring of reflection properties.** The annealing cell and heating block were placed under a microscope camera oriented perpendicular to the film and illuminated with a ring light. Images were captured at 4 s intervals and analyzed to extract sample color as 'hue' in the HSV color space using an image-analysis routine in MATLAB (code provided in ESI,† Section 4). To provide a dark (absorbing) background for reflection images, the bottom plate of the annealing cell was anodized black.

***In situ* monitoring of transmission properties.** The annealing cell and heating block were mounted in the sample compartment of a Cary 60 UV-Vis instrument (Agilent) and scanned from 300–700 nm at a rate of 3000 nm min^{-1} with scans performed every 12 s. An empty cell containing two glass slides was used as the background. To provide a path for the 1.5 mm × 1.0 mm beam, a hole was machined into the bottom plate of the annealing cell.

***Ex situ* reflection measurements.** Reflection spectra were collected using an integrating sphere attachment for a Varian Cary 5G UV-Vis-NIR instrument using a Spectralon standard.

d. Scanning electron microscopy and cross-section preparation

Well-defined cross-sections were prepared by freeze-fracturing films in liquid nitrogen. A razor blade was used to gently separate glass slides and cut and delaminate the polymer film to form high aspect-ratio slivers. These were then held at one end with copper tape and forceps and plunged into liquid nitrogen for several minutes before dragging another set of chilled forceps across the film to fracture. To reduce charging effects, all cross-section samples were coated with Au–Pd in an Emitech K575 sputter coater by sequentially mounting the sample vertically (fractured edge-facing up) and at 45 degrees for a total of two ~10 nm coating cycles. Imaging was performed using either the Hitachi S4800 or JEOL JSM-7000F Analytical SEM at the Illinois Materials Research Laboratory. Images were obtained at low accelerating voltages ($\leq$ 5 kV). Orientation analysis was performed by first pre-processing and binarizing images in FIJI/ImageJ2[50] and then using a slightly modified version of Persson, *et al.*'s GTFiber program[51] Further details are provided in ESI,† Section 5.

e. Small-angle X-ray scattering (SAXS)

Films investigated *via* transmission small-angle X-ray scattering were prepared by annealing as described above, except that solvent-washed polyimide sheets (Kapton – American Durafilm) were used in between the glass slides. SAXS measurements were performed at Argonne National Laboratory (Lemont, IL), on beamline 12-ID-B of the Advanced Photon Source, with a beam energy of 13.3 keV, and a Pilatus 2M 2D detector with source-detector-distance of 3.6 m. A silver behenate standard was used for q-calibration and data reduction was performed using the Nika package by J. Illavksy[52] in Igor Pro (WaveMetrics). Lamellar *d*-spacing was determined by simultaneous fitting of the inter-peak spacing of four diffraction orders using the LMFIT package in python.

III. Results

Thermal annealing and optical property evolution

Upon thermal annealing at temperatures beyond the glass transition temperature of both blocks, as-synthesized PS-*b*-PLA bottlebrush diblock copolymers rapidly undergo microphase separation with visible color change (Fig. 1b). During annealing, images were taken for a series of films ranging in thickness from 49.1 to 303.9 μm *via* a microscope camera mounted at normal incidence and illuminated with a ring light, capturing the progression of structure color from initially deep blue through a steady redshift to a final red-orange color (Fig. 1b). Films exhibited a center 'spot' which varied in size and appeared different in color to the broad, uniform edge region

which occupied > 80% of the visible sample area. Aside from collection of combined specular/diffuse UV-Vis reflection spectra, all *in situ* and *ex situ* measurements in this manuscript specifically sample only the uniform edge regions. During the final minutes of annealing, a dark, colorless ring creeps inwards from the edge of the film – a phenomenon we attribute to polymer degradation as opposed to further red shift of reflected wavelength, as none of the films studied show measurable infrared reflectance (ESI,† Section 6). PLA is known to be moisture and temperature sensitive, and we anticipate that the combination of heating and ambient humidity leads to degradation through hydrolysis of the PLA brushes to form lactic acid.[53,54]

Quantitative analysis of film color over time was performed *via* a MATLAB image processing script. To approximate the change in reflected color as a single parameter, the measured red, green, and blue intensity values for each pixel were converted to the HSV (hue, saturation, and value) scale. In this color model, the hue parameter predominately captures the spectral composition of the color, while saturation and value reflect the color purity and brightness, respectively.[55] Hue values were averaged frame by frame and tracked over the 10 minutes annealing time (Fig. 1c). For all samples, hue *versus* time curves evolve in two stages. First, an initial, rapid decrease in hue occurs over the course of less than 30 s from onset, followed by a more gradual decrease to the final stable value. In all cases, the rate of change of hue levels off well before 10 minutes has occurred. We find no systematic variation in inductance time before the transition.

In a complementary *in situ* experiment, we probed the transmission properties for a series of films spanning the same thickness range (Fig. 1d). Data were collected by taking sequential UV-Vis transmission measurements over the course of annealing. Although these data are expressed in terms of absorbance, both polystyrene and poly lactic acid are transparent within the visible spectrum, allowing us to attribute the measured 'absorbance' to deflection of light out of the beam path by reflection from internal BBCP domain interfaces. Beginning with the 47.0 μm thick sample, we observe the initial absence of a clear absorption peak, followed by appearance and progressive redshift of a peak over the course of annealing. Peak intensity does not substantially vary over time, although the width does gradually narrow. In thicker films (118.3 μm and 296.7 μm), we observe a similar redshift of the primary peak, however there is a region of broad absorption at all wavelengths below the primary peak. For the 296.7 μm film, this region between 350 nm and 550 nm is nearly totally flat.

The optical properties of the films after annealing are presented in Fig. 2, beginning with images of samples annealed under the microscope camera (Fig. 2a). Considering the color of each sample individually, there are generally three distinct regions. Near the center of the film, a weakly colored spot appears at the locations where the original BBCP powder fused together. This is surrounded by a broad region of much more uniform yellow/orange coloration, although there are minor patches streaks of color/brightness variation. The thickest film considered (304 μm), was found to exhibit substantial variation in color on the top surface of the film, although the bottom surface appearance (inset in Fig. 2a) was more consistent with the rest of the series.

Normalized reflection and transmission spectra, along with the results of peak fitting are shown in Fig. 2b–d. The measurement area for reflection spectra encompassed the entire film, and raw reflectivity values at the band gap center are as high as 80% *versus* a Spectralon (PTFE) standard (ESI,† Section 6). Transmission spectra probe a 1.5 mm × 1 mm spot contained within the uniform region of each sample. For all samples, both reflection and transmission spectra contain a primary Gaussian peak centered between 560–570 nm, with a broad plateau at lower wavelengths. The full-width half-max (FWHM) of the primary peak is in all cases is quite large (greater than 60 nm). In reflection mode there is an apparent minimum at intermediate thicknesses, while in transmission mode the FWHM monotonically increases with film thicknesses. In both reflection and transmission, as film thickness increased, the plateau at low wavelength increased substantially. Particularly for the 296.7 μm thick sample, the absorbance profile below the peak wavelength is nearly flat, with broad filtering of all wavelengths in the range of 350 nm to 580 nm.

Scanning electron microscopy and orientation analysis

The well-defined lamellar microstructure of samples prepared by thermal annealing were directly observed by cross-sectional scanning electron microscopy (Fig. 3). A section of each of the films prepared on the microscope stage was fractured in liquid nitrogen to prepare cross sections. For each film, a series of SEM images were taken in a trajectory that began at the film surface (substrate interface) and proceeded across the depth of the film until at least the film center. Fig. 3a contains stitched, contrast-enhanced micrographs encompassing a region of 6 μm in width by 34.8 μm in depth which extends from the substrate interface to the film center for a 69.0 μm thick BBCP film, directly visualizing the transition from large, well aligned grains near the substrate, to smaller orientationally disordered grains near the center.

Quantitative assessment of the film structure by image analysis was performed to map domain orientation and calculate an overall 2D orientational order parameter (S_{2D}, eqn (1)) for each SEM image.

$$S_{2D} = 2\langle\cos^2\theta_n\rangle - 1 \quad (1)$$

Here, S_{2D} is calculated after first binarizing and skeletonizing domains as individual fibers. The angle (θ_n) is computed as the difference between the local director vector calculated at each fiber pixel (n) and the average director of the entire image. S_{2D} ranges from 0 to 1, corresponding to a totally isotropic population of lamellae and perfect uniaxial alignment, respectively.[51] In Fig. 3b, we show representative SEM images taken within the surface, transition, and bulk regions of the 69.0 μm film; the analyzed fibers were superimposed and

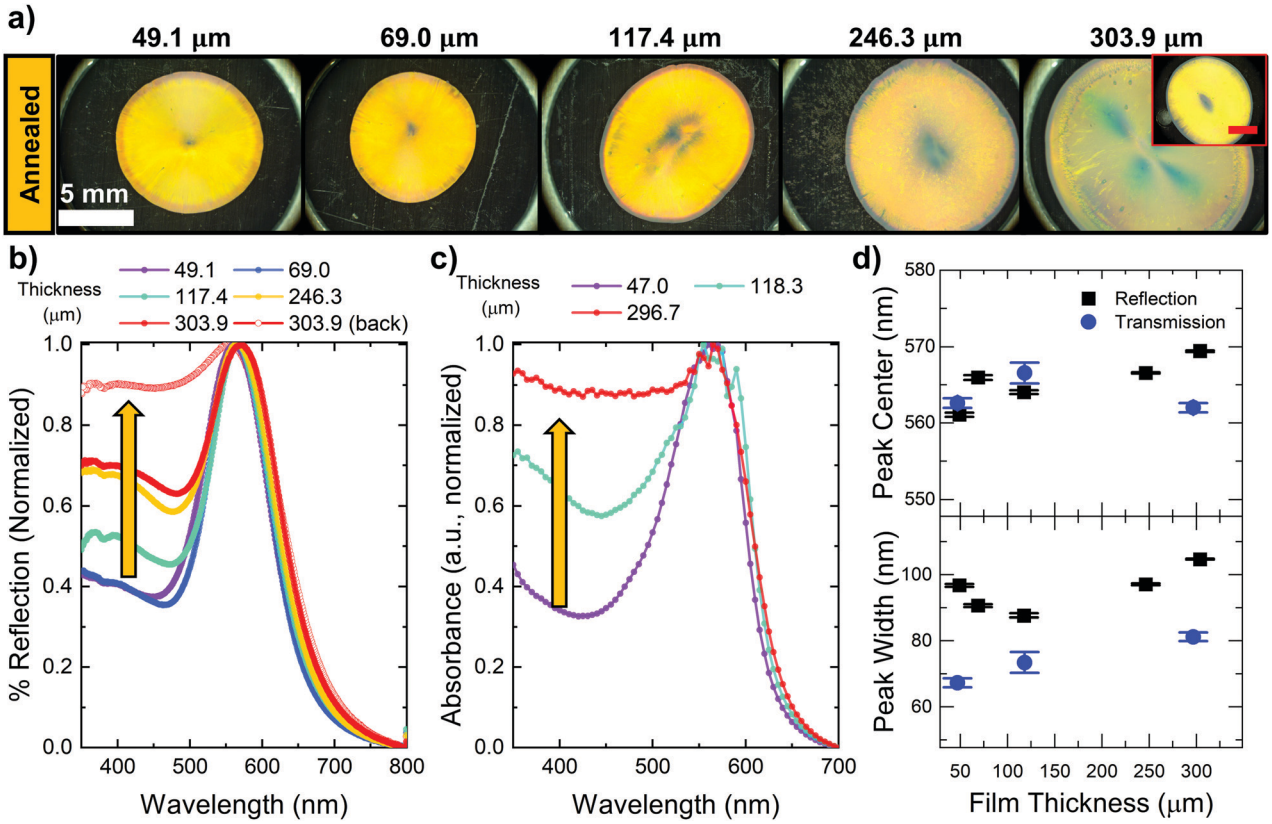

Fig. 2 Photonic properties of BBCP films after annealing. (a) Microscope camera images of samples of varying thickness after 10 minutes of annealing under normally incident light. The inset image of the 303.9 μm sample is the opposite (back) surface of the film. (b) Combined (diffuse + specular) reflection spectra for samples shown in panel a). Intensity data is normalized within the wavelength range of 350–800 nm. (c) Final absorbance spectra for a set of samples of varying thickness annealed within the UV-Vis spectrometer. Absorbance data is normalized between 350 and 700 nm. Arrow emphasizes the significant increase in off-peak reflectance with increasing film thickness. (d) Results of fitting optical peaks in reflection and transmission mode as symmetric or asymmetric Gaussian curves. For asymmetric peaks, the presented peak width is the sum of the widths of each side. Error bars reflect the standard error of the fit performed using the NLfit package in Origin 2021.

colorized by angle, showing high accuracy of the domain mapping approach. As highlighted by the pole figures, this method captures the distinctly different domain orientation distributions in each region. S_{2D} *vs.* depth data from two non-overlapping trajectories of SEM images traversing the entire film thickness of 69.0 μm are consistent (Fig. 3c), supporting the robustness of this approach. There is a clear quantitative difference between the orientation parameter in the regions visually identified as the interfacially aligned, transition, and bulk regions (arrows in Fig. 3c correspond to images in Fig. 3b). The same image analysis routine was applied to SEM image trajectories for films of varying thicknesses (Fig. 3d and ESI,† Videos) and reveals qualitatively similar behavior. In all cases, the orientation parameter near the substrate is quite high (more than 0.8), begins to abruptly decrease in the transition region, and substantially decreases near the film center to values less than 0.3. The clearest trend across the thin-thick samples is that the steepness of the transition between highly oriented regions and the orientationally disordered bulk substantially decreases with increasing film thickness (Fig. 3d). The propagation depth of the highly oriented region varies stochastically across the samples, but in all cases exceeds 60 layers (30 lamellar periods), and in the case of the 69.0 μm sample even spans ~200 layers (100 lamellar periods).

Transmission small-angle X-ray scattering (SAXS)

SAXS data provide statistically averaged sampling of the BBCP film microstructure over a much larger volume than electron microscopy. A series of samples spanning the same thickness range were prepared by annealing between polyimide sheets and probed with a beam tall enough to encompass the entire film thickness. 2D scattering data (Fig. 4a) indicate clear structure factor peaks with broad azimuthal smearing of peak intensity. To evaluate the average lamellar period (D_0) for each sample, 1D profiles (Fig. 4b) were obtained from linecuts. By evaluating D_0 from vertical linecuts, the population of lamellae oriented closest to perfectly parallel to the substrate are sampled. Sharp well-defined peaks were observed with constant inter-peak spacing, indicative of long-range lamellar ordering. Because the first order (n = 1) lamellar peak was obscured by the beamstop, D_0 for each thickness was obtained by simultaneous fitting of the inter-peak distance for peak orders 2 through 5. D_0 was found to be nearly insensitive to overall film thickness, with an average

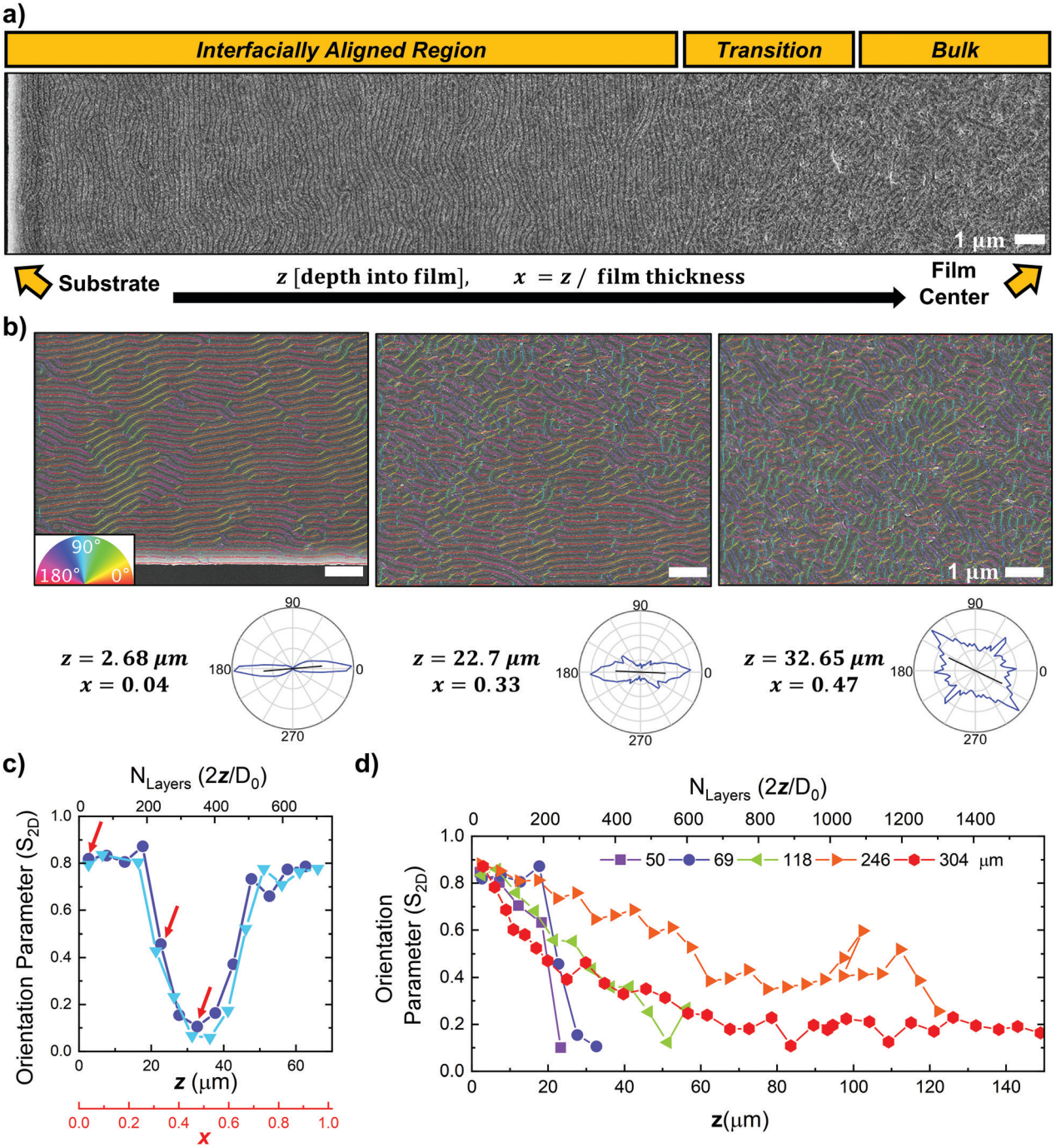

Fig. 3 Analysis of lamellar orientation from cross-sectional SEM images for a series of thick PS-*b*-PLA BBCP films. (a) From left to right edge: a stitched series of contrast-enhanced cross-sectional SEM images spanning the region from the film surface (substrate interface) to the film center (bulk) for a 69 μm thick film. (b) Individual SEM images taken at different depths into the film, overlaid with colorized fibers indicating local domain orientation. Each SEM image covers a region of 8.47 μm × 6.35 μm and is aligned such that the bottom boundary of the image is parallel to the substrate interface. Film depth is labeled in terms of distance from the substrate interface to the center of the image in both microns (z) and dimensionless units (x = z/film thickness). Pole figures are plotted from the orientation distribution of the colorized fibers shown. (c) Calculated 2D orientation parameter plotted *versus* scan depth for non-overlapping cross-sectional scan trajectories on the 69 μm thick film. The number of layers (N_{Layers}) labeled above is determined with respect to the average lamellar d-spacing (D_0) determined by SAXS. (d) Orientation parameter *versus* scan depth for a series of samples with varying film thickness. For visual clarity, data are shown only until the midpoint of each film and connected by straight lines.

value of 187.1 ± 2.1 nm (Fig. 4c). In all cases, the 1D plots of azimuthal intensity for the n = 3 peak for each film (Fig. 4d) indicate that a broad distribution of lamellar orientations is present.

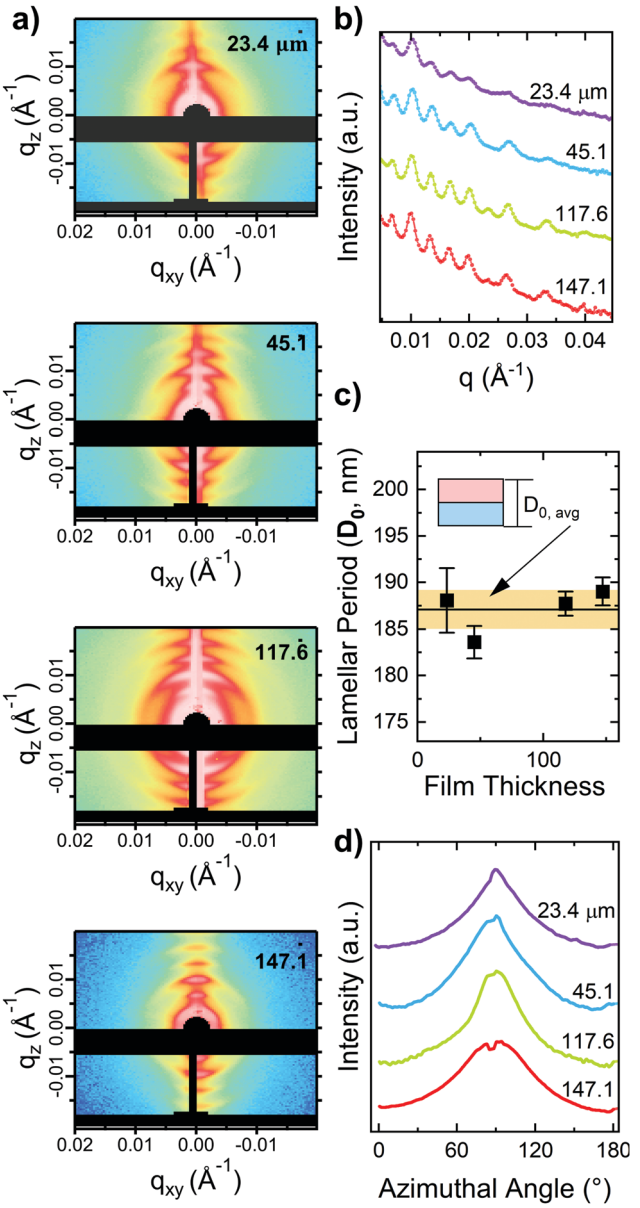

Fig. 4 Transmission Small-angle X-ray Scattering (SAXS) Characterization of BBCP Films. (a) 2D SAXS data taken with the beam encompassing the entire thickness of each film show clear lamellar stacking peaks with intensity spread over a substantial arc in the azimuthal direction. (b) 1D SAXS data obtained from vertical linecuts showing well-defined peaks at constant spacing (indicative of lamellar ordering). Intensity is plotted on log scale and curves are vertically shifted for clarity. (c) Lamellar period (*d*-spacing, d_0) calculated by simultaneous fitting of interpeak distance for peak orders 2 through 5. Error bars indicate the uncertainty of the fit. The average *d*-spacing and standard deviation (187.1 ± 2.1 nm) are noted by the horizontal black line and shaded rectangle, respectively. (d) 1D Azimuthal intensity data extracted from the n = 3 peak for each film. Intensity is plotted on log scale and curves are vertically shifted for clarity. For the 23.4 μm sample, the azimuthal angle is corrected for macroscopic sample tilt.

IV. Discussion and conclusions

We begin by providing a comprehensive picture of the microstructure of annealed films through a detailed discussion combining the results of cross-sectional SEM analysis, transmission SAXS, and *ex situ* optical measurements. Then, we use the results of our *in situ* measurements to propose a mechanism of competitive growth between lamellar grains heterogeneously nucleated at the surface and those homogeneously nucleated in the bulk.

As expected for BCP films prepared on a non-neutral substrate, a clear interfacially oriented region forms near both interfaces during annealing, which transitions to an orientationally disordered bulk near the film center. A detailed perspective on the local microstructure can be drawn from the cross-sectional SEM images, such as Fig. 3a and b and the ESI,† Videos, which contain composited colorized SEM image trajectories for each film thickness. As shown in the colorized images in Fig. 3b, the grain size in the interfacially oriented region is substantially larger than in the orientationally disordered bulk, with lateral dimensions exceeding several microns. While the interfacial region does exhibit strong alignment, the film is still substantially defective, with frequent dislocations, meandering domains, and the occasional presence of large ($\approx 4^*D_0$), substantially misaligned grains (tilted up to $\sim 30^\circ$) occurring even within a few periods of the substrate interface.

The decay of domain alignment with distance from the interface is quite complex. The profile is nearly symmetric about the film center (Fig. 3c), as expected for alignment induced by identical substrates. When comparing across several samples of different film thickness (Fig. 3d), in all cases the highly oriented interfacial region ($S_{2D} > 0.8$) propagates for greater than 30 lamellar periods before decaying to a substantially orientationally disordered bulk ($S_{2D} < 0.3$). The propagation depth of the interfacial region ranges from approximately 30 lamellar periods for the thickest film (304 μm) to a high of nearly 100 lamellar periods for one of the thinnest (69 μm), although there is no consistent trend with film thickness, likely due to the stochastic nature of lamella nucleation. There is a clear change in the sharpness of the transition, with thicker films exhibiting a much more gradual decay in orientation parameter than thinner films. We discuss this point further below.

SAXS data allow us to evaluate microstructural parameters averaged over a much larger volume of the film. Here we have obtained scattering data using a beam sized to probe the entire film thickness. All samples exhibiting regularly spaced peaks in intensity *versus* q (Fig. 4a and b) indicative of formation of lamellar domains. Evaluation of domain period from vertical linecuts gives an average value of 187.1 ± 2.1 nm across all film thicknesses (Fig. 4c). The narrow standard deviation is expected, as these film thicknesses are large enough that confinement effects[56] are not expected to lead to meaningful chain compression or stretching. The observed azimuthal variation in scattering intensity (Fig. 4d) is consistent with the local picture from SEM cross-sections. Peak intensity is spread over a substantial azimuthal range but is sharply enhanced along the vertical (q_z) axis, reflecting the larger proportion of lamellae oriented parallel to the substrate. The increased number of diffraction orders visible along the vertical

axis also provides evidence for the larger size of substrate-parallel grains.

Because the structural color reflected by high molecular weight BBCP arises from the interaction between incident photons and the periodic modulation of refractive index within the film, analysis of the film's photonic properties provides a useful probe of microstructure. To inform the following discussion we first briefly summarize the relationship between optical properties and film characteristics by comparison to an ideal 1D lamellar photonic crystal (Bragg stack[22,57]). Eqn (2), (3),[58] and eqn (4) relate the peak reflected wavelength (λ), bandwidth ($\Delta\lambda$), and the reflectivity (R), respectively, to the refractive index (n), layer thickness (d), and number of layers (N).

$$\lambda = 2(n_1 d_1 + n_2 d_2) \quad (2)$$

$$\Delta\lambda \approx \frac{4}{\pi}(d_1 + d_2)|n_2 - n_1| \quad (3)$$

$$R = \left[\frac{1 - \left(\frac{n_2}{n_1}\right)^{2N}}{1 + \left(\frac{n_2}{n_1}\right)^{2N}}\right]^2 \quad (4)$$

The simplified forms shown above are derived for normally incident light and (for eqn (3)) assume only small differences between n_1 and n_2 and d_1 and d_2. We judge this to be a good approximation in this case, based on the literature values for refractive index of polystyrene (1.592) and polylactic acid (1.461) at 560 nm, and calculation of the volume fraction of PS as $\phi_{PS} = 0.56$ (ESI,† Section 7). We note that the bandwidth specified in eqn (3) represents the minimum bandwidth for a perfect lamellar crystal. Peak broadening beyond this minimum is commonly attributed to different types of disorder such as block thickness variation, defects, or overall lamellar tilt. Lamellar tilt can also can substantially shift the reflectivity band to higher frequencies (lower wavelength).[57]

The measured photonic properties of the films after annealing are in excellent agreement with the *ex situ* microstructural characterization. From the cross-sectional scanning electron micrographs, the highly oriented interfacial region propagates for $>$ 30 domain periods. From eqn (4), a perfect 1-dimensional photonic crystal comprising 60 layers would reflect over 99.9% of normally incident light. Thus, we can expect the reflection properties of films to be dominated by the domains near the surface. In fact, evaluating eqn (2) with the average spacing determined by SAXS results in a predicted band gap centered on 574.3 nm, in excellent agreement with the measured peak reflection wavelengths of 561.1 to 569.4 nm (Fig. 2d). The increase in off-peak absorbance is also consistent with the observed film microstructure. Because transmission-mode measurements probe the entire film thickness, and thicker films contain more of the orientationally disordered region, increasing thickness means that incident photons of all wavelengths below the peak wavelength are much more likely to encounter domains tilted at angles that prohibit wave propagation, and are thus reflected out of the path of the detector. Finally, the photonic bandwidth measurements confirm that all films contain substantial disorder, with measured full-width half-max values ranging from 67.3 nm to 104.7 nm, far greater than the predicted bandwidth for a perfect 1D photonic crystal ($\approx$ 31 nm by eqn (3)).

We now discuss the rapid evolution of photonic properties early in the annealing process in the context of eqn (2)–(4) and propose a mechanism for the formation of the observed microstructure (Fig. 5). At the start of annealing, all films appear to be faintly blue in reflection mode and lack a clear absorption peak in transmission mode. These weak photonic properties can be directly linked to the disordered microstructure of the

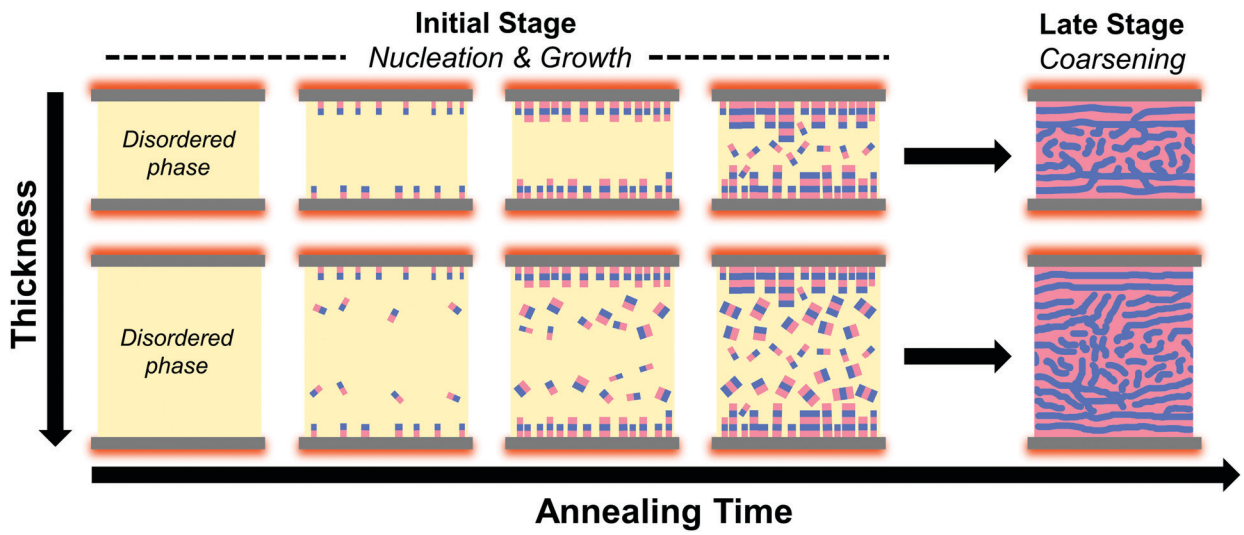

Fig. 5 Schematic of domain nucleation and growth during annealing. In each case, heterogeneously nucleated grains from the surfaces form and coarsen more rapidly than homogeneously nucleated grains in the bulk. In thicker films, the larger volume leads to earlier onset of nucleation and increased nucleation rate in the bulk while maintaining the nucleation rate induced by surfaces.

films prior to annealing, as indicated by cross-sectional scanning electron micrographs (ESI,† Section 8). As previously described, the wavelength (color) of reflected light is primarily governed by domain thickness (eqn (2)) and orientation,[57] while the reflected intensity is additionally impacted by refractive index contrast and the number of layers (eqn (4)). Block copolymers in the disordered state are not compositionally uniform and are instead characterized by short range compositional fluctuations with broad interfacial width.[1] For this BBCP system, the PS/PLA compositional fluctuations are of sufficient length scale as to lead to reflection of blue wavelengths. The low reflected intensity prior to annealing is likely due to a combination of two factors: (1) the suppression of constructive interference of reflected light due to the randomness of PS/PLA interfacial orientation and (2) poor refractive index contrast due to the large interfacial widths.

Within minutes of heating beyond T_g of both blocks, the samples' reflected color rapidly red-shifts and reflected intensity increases, before stabilizing and changing little for the remainder of the annealing time (Fig. 1c). Here, the increase in the wavelength of reflected light has contributions from both (1) the formation of lamellar domains whose domain size increases to minimize interfacial area, and (2) the re-alignment of domains to be more parallel to the interface. The increased reflected intensity can be linked to both the incorporation of additional layers into the photonic crystal, and to a lesser extent by the increase in domain purity (refractive index contrast) that occurs during microphase separation.

With these links between evolving photonic properties and microstructure established, we can propose the mechanism for the observed final microstructure that is consistent with established theory on microphase separation and grain coarsening during annealing of block copolymer films from an initial quenched disordered state.[4,59] Because annealing occurs at a temperature well below the order–disorder transition temperature, the driving force for domain nucleation and growth is high, and in the early stages of annealing, grains can grow rapidly by incorporating nearby chains from the surrounding disordered regions. Once the volume is saturated with domains, further grain coarsening slows considerably, and is achieved by defect elimination. As discussed earlier, the reflection-mode measurement of hue is primarily surface-sensitive, and so we infer that the rapid color change observed for all samples (Fig. 1b and c) is dominated by heterogeneous nucleation of substrate-parallel lamellae at the polymer-glass interface, and their rapid growth and coarsening into larger grains. By contrast, the slower formation and shift of the broad, thickness-dependent absorption feature is attributed to the formation, coarsening, and realignment of the randomly oriented grains that nucleate homogeneously within the bulk of the polymer films.

The full microstructure of the films is complex, with grain size and orientation varying as a function of film depth, along with a change in the sharpness of the decay in the orientational order parameter S_{2D} with increase film thickness (shown in Fig. 3d). In all cases, there is a transition between large, substrate-aligned grains near the glass-polymer interface and small, isotropically oriented grains near the film center. In thinner films, the transition is sharp, while in thicker films it occurs gradually, across a large portion of the film. A possible mechanism for the formation of this morphology can be proposed by considering the nucleation and growth process. We suspect that the very early stages of annealing, where the film transitions from disordered to ordered play a major role in determining the observed microstructure.

We infer that the microstructure observed is a result of competing heterogenous nucleation at the substrate interfaces *vs.* homogenous nucleation in the bulk of the film. Heterogeneous nucleation of substrate-parallel domains is expected to occur first, given the lower free energy barrier for surface-induced nucleation. The thus-formed lamella domains can then rapidly propagate inwards through the disordered melt in the bulk. As the phase front propagates, homogeneous nucleation may occur throughout the remaining bulk disordered phase, leading to formation of isotropically oriented domains. Because homogeneous nucleation is volume dependent, it occurs later in the annealing process, with fewer nucleation sites for thinner films, leading to a sharp transition between the heterogeneously aligned grains and the isotropic grains (upper row of Fig. 5). In thicker films, multiple homogeneous nucleation events are likely to occur earlier in the annealing process. The homogeneous grains that nucleate earlier can themselves grow into the disordered phase, interfering with the propagation of substrate-parallel domains and leading to more gradual decay of orientation parameter (lower row of Fig. 5).

In summary, the key conclusions of this manuscript are as follows:

1. During conventional thermal annealing of thick films of large (N_{bb} = 400) bottlebrush polymers, interface-directed assembly promotes extremely rapid (~minutes) formation of well-aligned grains which extends for up to 100 lamellar periods, far beyond the penetration of typical surface fields in linear block copolymers.

2. The degree of orientational order in thermally annealed thick films decays towards the film center, eventually reaching an orientationally isotropic bulk, and that the sharpness of the orientation gradient is strongly affected by the overall film thickness in the 10 s–100 s of micron regime.

3. The formation of the interfacially-aligned regions gives rise to the previously reported strong reflective properties of BBCP PC, while the differing width of the bulk isotropic region leads to variation of transmittance and leads to broadband filtering response for very thick (>100 micron) BBCP films.

Conflicts of interest

There are no conflicts to declare.

Acknowledgements

The authors would like to thank C. Sing, S. Rogers, M. Wade, T. Pan, and Y. Kamble of the Univ. of Illinois for intellectual

discussions regarding this work. Experiments were carried out, in part, in the MRL Central Research Facilities, University of Illinois. This research used resources of the Advanced Photon Source; a U.S. Department of Energy (DOE) Office of Science User Facility operated for the DOE Office of Science by the Argonne National Laboratory under contract no. DE-AC02-06CH11357. This work was supported by the NSF under DMREF award no. DMR-1727605. J.K. and Y.D. acknowledge partial support by the NSF CAREER award under grant no. NSF DMR 18-47828. Major funding for the 500 MHz Bruker CryoProbe was provided by the Roy J. Carver Charitable Trust to the University of Illinois School of Chemical Sciences NMR Lab. The authors thank Umicore for the generous gift of Grubbs Catalyst.

References

1 F. S. Bates and G. H. Fredrickson, *Annu. Rev. Phys. Chem.*, 1990, **41**, 525–557.
2 H. Yoshida and M. Takenaka, in *Directed Self-assembly of Block Co-polymers for Nano-manufacturing*, ed. R. Gronheid and P. Nealey, Woodhead Publishing, 2015, pp. 3–26.
3 C. M. Bates and F. S. Bates, *Macromolecules*, 2017, **50**, 3–22.
4 P. W. Majewski and K. G. Yager, *J. Phys.: Condens. Matter*, 2016, **28**, 403002.
5 J. A. Liddle and G. M. Gallatin, *ACS Nano*, 2016, **10**, 2995–3014.
6 A. P. Marencic and R. A. Register, *Annu. Rev. Chem. Biomol. Eng.*, 2010, **1**, 277–297.
7 H. Hu, M. Gopinadhan and C. O. Osuji, *Soft Matter*, 2014, **10**, 3867–3889.
8 R. A. Farrell, E. R. Hosler, G. M. Schmid, J. Xu, M. E. Preil, V. Rastogi, N. Mohanty, K. Kumar, M. J. Cicoria, D. R. Hetzer and A. DeVilliers, in *Manufacturability Considerations for DSA*, ed. T. I. Wallow and C. K. Hohle, San Jose, California, USA, 2014, p. 90510Z.
9 M. Christopher Orilall and U. Wiesner, *Chem. Soc. Rev.*, 2011, **40**, 520–535.
10 A. Haryono and W. H. Binder, *Small*, 2006, **2**, 600–611.
11 A. Alvarez-Fernandez, C. Cummins, M. Saba, U. Steiner, G. Fleury, V. Ponsinet and S. Guldin, *Adv. Opt. Mater.*, 2021, **9**, 2100175.
12 G. Polymeropoulos, G. Zapsas, K. Ntetsikas, P. Bilalis, Y. Gnanou and N. Hadjichristidis, *Macromolecules*, 2017, **50**, 1253–1290.
13 T.-P. Lin, A. B. Chang, S.-X. Luo, H.-Y. Chen, B. Lee and R. H. Grubbs, *ACS Nano*, 2017, **11**, 11632–11641.
14 W. F. M. Daniel, J. Burdyńska, M. Vatankhah-Varnoosfaderani, K. Matyjaszewski, J. Paturej, M. Rubinstein, A. V. Dobrynin and S. S. Sheiko, *Nat. Mater.*, 2016, **15**, 183–189.
15 J. Paturej, S. S. Sheiko, S. Panyukov and M. Rubinstein, *Sci. Adv.*, 2016, **2**, e1601478.
16 H. Liang, B. J. Morgan, G. Xie, M. R. Martinez, E. B. Zhulina, K. Matyjaszewski, S. S. Sheiko and A. V. Dobrynin, *Macromolecules*, 2018, **51**, 10028–10039.
17 W. Gu, J. Huh, S. W. Hong, B. R. Sveinbjornsson, C. Park, R. H. Grubbs and T. P. Russell, *ACS Nano*, 2013, **7**, 2551–2558.
18 G. H. Fredrickson and F. S. Bates, *Annu. Rev. Mater. Sci.*, 1996, **26**, 501–550.
19 D. F. Sunday, A. B. Chang, C. D. Liman, E. Gann, D. M. Delongchamp, L. Thomsen, M. W. Matsen, R. H. Grubbs and C. L. Soles, *Macromolecules*, 2018, **51**, 7178–7185.
20 Z. Cao, J.-M. Y. Carrillo, S. S. Sheiko and A. V. Dobrynin, *Macromolecules*, 2015, **48**, 5006–5015.
21 S. J. Dalsin, T. G. Rions-Maehren, M. D. Beam, F. S. Bates, M. A. Hillmyer and M. W. Matsen, *ACS Nano*, 2015, **9**, 12233–12245.
22 A. L. Liberman-Martin, C. K. Chu and R. H. Grubbs, *Macromol. Rapid Commun.*, 2017, **38**, 1700058.
23 C.-G. Chae, Y.-G. Yu, H.-B. Seo, M.-J. Kim, R. H. Grubbs and J.-S. Lee, *Macromolecules*, 2018, **51**, 3458–3466.
24 D.-P. Song, T. H. Zhao, G. Guidetti, S. Vignolini and R. M. Parker, *ACS Nano*, 2019, **13**, 1764–1771.
25 B. R. Sveinbjörnsson, R. A. Weitekamp, G. M. Miyake, Y. Xia, H. A. Atwater and R. H. Grubbs, *Proc. Natl. Acad. Sci. U. S. A.*, 2012, **109**, 14332–14336.
26 B. B. Patel, D. J. Walsh, D. H. Kim, J. Kwok, B. Lee, D. Guironnet and Y. Diao, *Sci. Adv.*, 2020, **6**, eaaz7202.
27 M. Vatankhah-Varnosfaderani, A. N. Keith, Y. Cong, H. Liang, M. Rosenthal, M. Sztucki, C. Clair, S. Magonov, D. A. Ivanov, A. V. Dobrynin and S. S. Sheiko, *Science*, 2018, **359**, 1509–1513.
28 M. A. Wade, D. Walsh, C.-W. Lee, E. Kelley, K. Weigandt, D. Guironnet and S. Rogers, *Soft Matter*, 2020, **16**, 4919–4931.
29 G. M. Miyake, V. A. Piunova, R. A. Weitekamp and R. H. Grubbs, *Angew. Chem., Int. Ed.*, 2012, **51**, 11246–11248.
30 R. J. Macfarlane, B. Kim, B. Lee, R. A. Weitekamp, C. M. Bates, S. F. Lee, A. B. Chang, K. T. Delaney, G. H. Fredrickson, H. A. Atwater and R. H. Grubbs, *J. Am. Chem. Soc.*, 2014, **136**, 17374–17377.
31 D.-P. Song, C. Li, W. Li and J. J. Watkins, *ACS Nano*, 2016, **10**, 1216–1223.
32 Q. He, K. H. Ku, H. Vijayamohanan, B. J. Kim and T. M. Swager, *J. Am. Chem. Soc.*, 2020, **142**, 10424–10430.
33 D.-P. Song, C. Li, N. S. Colella, W. Xie, S. Li, X. Lu, S. Gido, J.-H. Lee and J. J. Watkins, *J. Am. Chem. Soc.*, 2015, **137**, 12510–12513.
34 T. P. Russell, G. Coulon, V. R. Deline and D. C. Miller, *Macromolecules*, 1989, **22**, 4600–4606.
35 M. J. Fasolka and A. M. Mayes, *Annu. Rev. Mater. Res.*, 2001, **31**, 323–355.
36 E. Han, K. O. Stuen, M. Leolukman, C.-C. Liu, P. F. Nealey and P. Gopalan, *Macromolecules*, 2009, **42**, 4896–4901.
37 T. Xu, C. J. Hawker and T. P. Russell, *Macromolecules*, 2005, **38**, 2802–2805.
38 C. Shin, H. Ahn, E. Kim, D. Y. Ryu, J. Huh, K.-W. Kim and T. P. Russell, *Macromolecules*, 2008, **41**, 9140–9145.
39 S. Ji, C.-C. Liu, W. Liao, A. L. Fenske, G. S. W. Craig and P. F. Nealey, *Macromolecules*, 2011, **44**, 4291–4300.

40 C. K. Shelton and T. H. Epps, *Macromolecules*, 2016, **49**, 574–580.
41 T. Vu, N. Mahadevapuram, G. M. Perera and G. E. Stein, *Macromolecules*, 2011, **44**, 6121–6127.
42 X. Zhang, B. C. Berry, K. G. Yager, S. Kim, R. L. Jones, S. Satija, D. L. Pickel, J. F. Douglas and A. Karim, *ACS Nano*, 2008, **2**, 2331–2341.
43 D. J. Walsh, M. A. Wade, S. A. Rogers and D. Guironnet, *Macromolecules*, 2020, **53**, 8610–8620.
44 B. G. G. Lohmeijer, R. C. Pratt, F. Leibfarth, J. W. Logan, D. A. Long, A. P. Dove, F. Nederberg, J. Choi, C. Wade, R. M. Waymouth and J. L. Hedrick, *Macromolecules*, 2006, **39**, 8574–8583.
45 D. J. Walsh and D. Guironnet, *Proc. Natl. Acad. Sci. U. S. A.*, 2019, **116**, 1538–1542.
46 D. J. Worsfold and S. Bywater, *Can. J. Chem.*, 1960, **38**, 1891–1900.
47 R. Waack, A. Rembaum, J. D. Coombes and M. Szwarc, *J. Am. Chem. Soc.*, 1957, **79**, 2026–2027.
48 S. Breunig, V. Héroguez, Y. Gnanou and M. Fontanille, *Macromol. Symp.*, 1995, **95**, 151–166.
49 D. J. Walsh, S. Dutta, C. E. Sing and D. Guironnet, *Macromolecules*, 2019, **52**, 4847–4857.
50 C. T. Rueden, J. Schindelin, M. C. Hiner, B. E. DeZonia, A. E. Walter, E. T. Arena and K. W. Eliceiri, *BMC Bioinf.*, 2017, **18**, 529.
51 N. E. Persson, M. A. McBride, M. A. Grover and E. Reichmanis, *Chem. Mater.*, 2017, **29**, 3–14.
52 J. Ilavsky, *J. Appl. Crystallogr.*, 2012, **45**, 324–328.
53 M. A. Elsawy, K.-H. Kim, J.-W. Park and A. Deep, *Renewable Sustainable Energy Rev.*, 2017, **79**, 1346–1352.
54 V. Speranza, A. De Meo and R. Pantani, *Polym. Degrad. Stab.*, 2014, **100**, 37–41.
55 K. N. Plataniotis and A. N. Venetsanopoulos.
56 D. F. Sunday, M. Dolejsi, A. B. Chang, L. J. Richter, R. Li, R. J. Kline, P. F. Nealey and R. H. Grubbs, *ACS Nano*, 2020, **14**, 17476–17486.
57 A. C. Edrington, A. M. Urbas, P. DeRege, C. X. Chen, T. M. Swager, N. Hadjichristidis, M. Xenidou, L. J. Fetters, J. D. Joannopoulos and Y. Fink, *Adv. Mater.*, 2001, **13**, 421–425.
58 S. Kinoshita, S. Yoshioka and J. Miyazaki, *Rep. Prog. Phys.*, 2008, **71**, 076401.
59 H. J. Dai, N. P. Balsara, B. A. Garetz and M. C. Newstein, *Phys. Rev. Lett.*, 1996, **77**, 3677–3680.